Academic Journal of Science and Technology
ISSN: 2771-3032 | Vol. 20, No. 3, 2026

Thermal Characterization and Simulation of the Iron Ore Sintering Process

Yuxuan Wang[a], Haoyuan Deng, Haoxuan Sun, Yuhan Zhang, Bin Bai[*]

School of Science, North China University of Science and Technology, Tangshan, Hebei 063000, China
[a]wyx830013@163.com, [*] **Corresponding author**: baibin1028@126.com

Abstract: Accurately identifying the state of the sintering process and stably controlling the sintering endpoint are fundamental challenges that cannot be bypassed in the iron ore sintering process .In this study, by analyzing the temperature and concentration of flue gas emitted during the four stages of preheating, combustion, sintering, and cooling in the sintering process, optimizing the parameters of the Gaussian emission distribution using forward-backward and Baum-Welch algorithms, and dynamically tracking the transition path of the sintering thermal state using a Viterbi decoding strategy, a numerical characterization method for sintering states based on a Gaussian HMM model is proposed. The computational results indicate that the model demonstrates high discrimination capability across the preheating, sintering, and cooling stages, with F1 scores all exceeding 0.98. The model achieves a calculation accuracy of up to 96.63% for sintering thermal states, providing reliable support for the accurate identification of thermal states during the sintering process.

Keywords: Thermal state of iron ore sintering; Gaussian HMM model; forward-backward algorithm; Baum-Welch algorithm; Viterbi algorithm.

1. Introduction

Iron ore sintering refers to a thermal agglomeration process in which iron ore powder, recycled ironmaking products, fluxes, slagging agents, and solid fuel (coke) are mixed and placed in a sintering machine for ignition and combustion, ultimately sintering into lumps [1]. This process is accompanied by physicochemical phenomena such as phase transitions, heat and mass transfer, fluid flow, combustion, and mineral formation and transformation, and exhibits characteristics such as nonlinearity, time-varying behavior, significant time delay, and strong coupling [2] .

The thermal state of sintering is a critical process parameter in the iron ore sintering process and a key factor influencing the green, low-carbon, and high-quality production of sintered ore. Identifying the mechanisms of thermal agglomeration in iron ore sintering, accurately determining the state of the sintering process, stably controlling the sintering endpoint, and optimizing the sintering production process to make it more low-carbon and intelligent have become pressing issues in iron ore sintering technology. In actual production, the sintering process is complex, the on-site environment is harsh, and detection methods are limited. Without specific measures to accurately obtain thermal state parameters during the sintering process, constructing mathematical models based on data from the sintering machine's air boxes is a commonly used method to assist in controlling the sintering production process. Long Hongming [3] described the thermal state of the sintering process in terms of the distribution of bed thickness across different zones and the variation in migration velocity. Using a non-contact infrared temperature scanner to measure the vertical temperature of the sintering machine car side panels, they established a model for dividing the bed into zones, calculated the thickness and migration velocity of each zone, and analyzed their thermal characteristics. Jing Kai et al. ([)4] proposed an ANFIS-based model for predicting the sintering endpoint, incorporating principal component analysis into the model construction and conducting simulation tests. The test results indicate that the model possesses good learning and adaptive capabilities. Wang Hongwen et al. ([)5] applied cutting-edge technologies such as wavelet analysis and artificial intelligence to actual sintering production processes, pointing out that wavelet analysis time-series algorithms can further optimize sintering prediction capabilities, effectively suppress fluctuations in the sintering endpoint, and improve the calculation accuracy of the sintering endpoint. Wang Bin et al. ([)6] described the kinetic characteristics of the sintering process based on interval numbers, established a two-dimensional interval autoregressive model with inputs, and improved the accuracy of sintering state prediction. Wang Fubin et al. ([)7] pointed out that the average car speed is a key parameter affecting the stability of sintering production, focused on analyzing the relationship between car speed and critical sintering temperature, and constructed a sintering behavior model. Yang et al. ([8])utilized an Autoformer to perform sequence correlation analysis on sintering process monitoring data, thereby implementing soft measurement of the sintering process. Fan Xiaohui et al. ([9])reviewed intelligent control models for predicting sintering states from the perspective of sintered ore quality. Yang Jing et al. ([10])constructed an online prediction system for intelligent identification and quality inspection of sintering operations using data learning and multi-information fusion techniques.

To further accurately infer the transition process of sintering states, this paper proposes a numerical characterization method for sintering states based on a Gaussian HMM model. This study integrates the temperature and concentration of flue gas emitted during the four stages of the sintering process—preheating, combustion, sintering, and cooling—across multiple dimensions. It optimizes the parameters of the Gaussian emission distribution using forward-backward and Baum-Welch algorithms, and employs a Viterbi decoding strategy to dynamically track the transition path of the sintering thermal state, thereby providing reliable support for the accurate identification of the thermal state

during the sintering process.

2. Sintering State

The iron ore sintering production process involves mixing various iron ores, flux agents, and solid fuels (coke) into granules and feeding them into the sintering machine. Subsequently, ignition occurs on the surface of the bed, while the air box beneath the sintering machine begins to draw air to create a certain degree of negative pressure, Air flows from top to bottom through the sintering bed into the lower air chamber, causing the solid fuel to gradually ignite from top to bottom and generate sufficient heat (around 1300°C). The flame front moves downward through the mixture, sintering the particles together to form a porous clinker known as sintered ore.

After ignition, the flame front moves downward through the material bed under the influence of the draft as the upper fuel is consumed. The temperature within the material bed first rises and then falls. Based on changes in the material bed during the sintering process, it is roughly divided from top to bottom into the sintered ore layer, combustion layer, preheating and drying layer, over-moisture layer, and sintering material layer. Sintering is complete when the combustion layer reaches the grate. As shown in Figure 1 below:

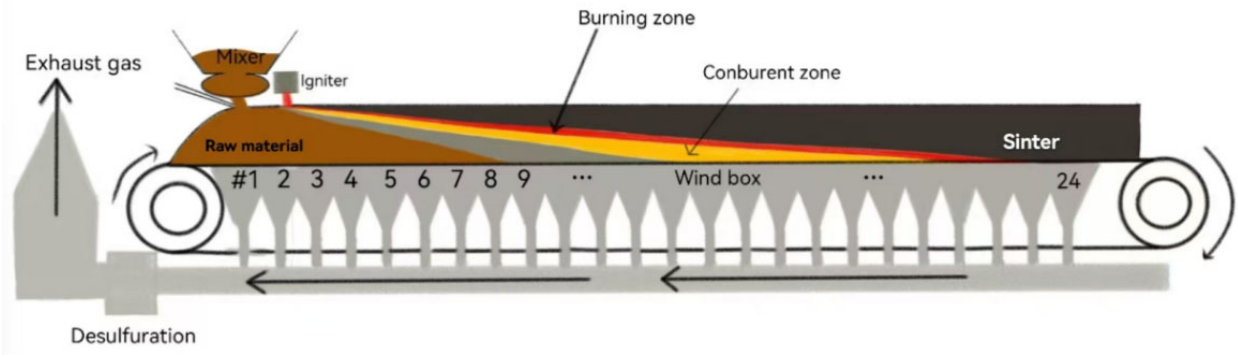


Figure 1. Schematic Diagram of the Iron Ore Sintering Process

The states of the sintering process primarily refer to the permeability state and thermal state of the material bed during iron ore sintering. Permeability refers to the ease with which gases can pass through the solid material bed; the flow state of gases within the sintered material bed is related to mass transfer, heat transfer, and physicochemical reactions during the sintering process. The thermal state, also known as the temperature state, can be characterized by three key parameters: the temperature rising point (TRP), the burn rising position (BRP), and the burn-through point (BTP) ([9]).

3. Characteristics of Sintering Flue Gas Emissions

In iron ore sintering, based on the evolution of the five material layer structures—the sintered ore zone, combustion zone, drying and preheating zone, over-moisture zone, and raw material zone—the sintering process can be further categorized into six characteristic states: State I, where ignition begins and the combustion zone and drying/preheating zone form; State II, which includes the five material layer structures; State III, where the raw material zone disappears; State IV, where the over-moisture zone disappears; State V, where the drying/preheating zone disappears; and State VI, where the combustion zone disappears. The emission characteristics of flue gas mass concentration in each sintering state are shown in Figure 2.

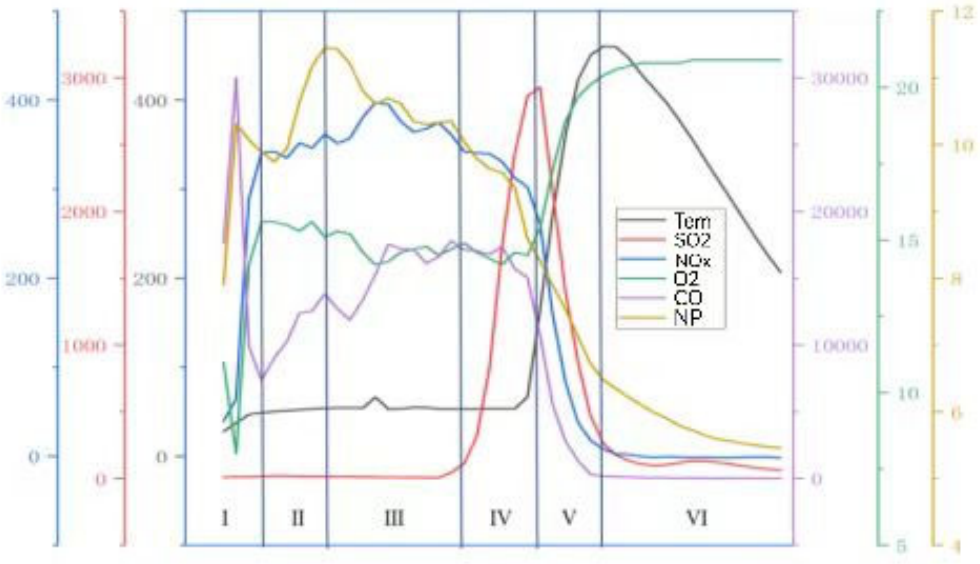


Figure 2. Correlation between flue gas emission patterns and the sintering state transition process

When the sintering process is in State I, as the sintering ignition proceeds, the combustion zone and the drying/preheating zone gradually form and thicken. The combustion reaction becomes increasingly intense, generating more flue gas, and the mass concentration rises sharply to a significant peak. After ignition ends, a large volume of air enters the sintered bed with the negative-pressure exhaust, strengthening the oxidizing atmosphere. As carbon burns completely, the mass concentration of CO drops rapidly again; When the sintering process is in Stage II, the thicknesses of the combustion zone and the drying/preheating zone remain constant. However, as vacuum sintering continues, the proportion of softened and molten material in the bed increases, the liquid phase of the sintered material expands, and the over-moisture zone gradually thickens. This reduces the permeability of the material bed, causing the negative pressure to reach its maximum value. The oxidizing atmosphere weakens, and the flue gas concentration rises to a high-concentration range; When the sintering process is in Stage III, the combustion process stabilizes, and the flue gas remains in the high-concentration range; When the sintering process is in Stage IV, the over-moisture zone gradually disappears, and $_{SO_2\ in}$the flue $_{gas}$is rapidly released, reaching a peak emission concentration; When the sintering process is in Stage V, the over-moisture zone completely disappears, the proportion of the sintered ore layer increases, the combustion zone and drying preheating zone gradually shrink, the permeability of the material bed improves significantly, the oxidizing atmosphere strengthens, carbon combustion becomes complete, and the mass concentration of the flue gas rapidly decreases; When the sintering process enters State VI, the combustion zone gradually disappears, sintering is completed, and the mass concentrations of all flue gas components gradually approach$^{0\ mg/m^3}$.

4. Sintered state Gaussian Hidden Markov Model characterization model

This section primarily introduces a numerical calculation model for iron ore sintering states based on the Gaussian HMM model, utilizing the Viterbi algorithm decoding strategy to dynamically track the transition paths of the sintering thermal state.

4.1. Gaussian HMM Data Characterization of Sintering States

In the iron ore sintering process, the six-dimensional observation signals—exhaust gas temperature, SO_2, NO, NO_x, O_2, and CO—exhibit characteristics such as multimodality, temporal correlation, and noise interference as the process progresses through its stages (preheating → combustion → sintering → cooling). To accurately identify the latent operating conditions in each stage, characterize emission dynamics, and provide decision support for carbon emission control, a time-series model is required that can both model hidden state transitions and handle continuous multidimensional observations. The Gaussian Hidden Markov Model [11,12] (Gaussian HMM) is an extension of the Hidden Markov Model, in which the observation probability distribution follows a Gaussian distribution (unimodal or multimodal). In the Gaussian HMM, the observation probability b_j(t) is no longer a discrete value but is defined by a Gaussian distribution. Each hidden state s_j corresponds to a Gaussian distribution:

$$b_j(o_t) = N(o_t|\mu_i, \Sigma_i) = \frac{1}{\sqrt{(2\pi)^k|\Sigma_j|}} \exp\left(-\frac{1}{2}(o_t-\mu_j)^T\Sigma_j^{-1}(o_t-\mu_j)\right)$$

This allows the mean $\mu_i$to capture the average emission characteristics of that stage, while the covariance $\Sigma_i$characterizes the dynamic interactions and uncertainty among various indicators. Parameter set of the Gaussian HMM emission distribution

$$B = \{(\mu_i, \Sigma_i)|i = 1,...,n\}$$

Therefore, in a Gaussian HMM, the probability formula for generating the observation sequence O = {o1, o2, ..., o_T} is:

$$P(O,\lambda) = \sum_S \left[\pi_{S1} \bullet \left(\prod_{t=1}^{T-1} a_{s_t s_{t+1}}\right) \bullet \left(\prod_{t=1}^{T} N(O_t|\mu_{S_t}, \Sigma_{S_t})\right)\right]$$

4.2. Model Solution

4.2.1. Model Solution

The study first reads minute-level flue gas monitoring data from the sintering process—including six parameters: temperature, SO_2, NO, NOx, O_2, and CO—using a Python script, and sorts the data in chronological order; maximum likelihood estimation (MLE) is then used to set the initial parameters of the Gaussian HMM model. Next, based on the Baum–Welch algorithm [13], the parameters of the Gaussian HMM were estimated iteratively until the log-likelihood gain fell below a preset threshold or the maximum number of iterations was reached; subsequently, the Viterbi algorithm [14] to decode the most likely state sequence, and predict the hidden state for each minute starting from a specified initial time until the first determination of the “cooling” phase. The specific solution process is as follows:

Step 1: Analyze and organize the sintering process exhaust gas monitoring dataset to establish an initial dataset.

Step 2: Apply the Random Forest algorithm to the initial dataset to impute missing and outlier data, thereby improving the efficiency and accuracy of the HMM model.

Step 3: By analyzing the correlation between carbon emission assessments of the sintering process and the Hidden Markov Model (HMM), the key stages of the sintering process (preheating, combustion, sintering, cooling) are incorporated as hidden states into the hidden layer, while the filtered monitoring data are incorporated as observable states into the observation layer. Maximum Likelihood Estimation (MLE) is used to set the initial HMM model parameters λ = (Π, A, B).

Step 4: Using the Baum-Welch algorithm, train the mean vector $\mu_i$and covariance matrix $\Sigma_{(i)}$ of the Gaussian emission distribution for each state to maximize the probability of the current observation data occurring, until the model parameters stabilize, thereby obtaining the optimal Hidden Markov Model.

Step 5: Using the trained model and the current known observation sequence, predict the most likely observation value for the next time step through probability calculations, and select the result with the highest probability as the prediction output. Finally, using the optimal model parameters obtained above and the new observation sequence V, apply the Viterbi algorithm to derive the optimal hidden state sequence S, and ultimately infer the cooling timing.

4.2.2. Model Training and Optimization:

(1) Since the Baum-Welch algorithm is highly sensitive to

initial values, the initial parameters λ = (Π, A, B) of the HMM model are set using maximum likelihood estimation (MLE).

$$\Pi = [1,0,0,0]^{T}$$

$$A = \begin{bmatrix} 0.9787 & 0.0213 & 0 & 0 \\ 0 & 0.8888 & 0.1112 & 0 \\ 0 & 0 & 0.9167 & 0.0833 \\ 0 & 0 & 0 & 1 \end{bmatrix}$$

After normalization, the MLE estimates yield the transition distribution B, specifically the mean vector $\mu_i$and the covariance matrix $\Sigma_i$of the Gaussian transition distribution for each state:

$$\mu_0 = \begin{pmatrix} -0.8353 \\ -0.2483 \\ 0.8026 \\ 0.8097 \\ -0.7966 \\ 0.8023 \end{pmatrix} \mu_1 = \begin{pmatrix} 0.2229 \\ 2.3957 \\ 0.0819 \\ 0.0263 \\ -0.1443 \\ -0.0346 \end{pmatrix} \mu_2 = \begin{pmatrix} 1.6583 \\ -0.1314 \\ -1.1205 \\ -1.1187 \\ 1.1067 \\ -1.1108 \end{pmatrix} \mu_3 = \begin{pmatrix} 0.8263 \\ -0.3958 \\ -1.1912 \\ -1.1842 \\ 1.2123 \\ -1.1460 \end{pmatrix}$$

$$\sum_0 = \begin{pmatrix} 0.001220 & 0 & 0 & 0 & 0 & 0 \\ 0 & 0.506051 & 0 & 0 & 0 & 0 \\ 0 & 0 & 0.231292 & 0 & 0 & 0 \\ 0 & 0 & 0 & 0.232077 & 0 & 0 \\ 0 & 0 & 0 & 0 & 0.222268 & 0 \\ 0 & 0 & 0 & 0 & 0 & 0.266865 \end{pmatrix}$$

denoted as:

Σ_0 =diag(0.001220,0.506051,0.231292,0.232077,0.222268,0.266865)

Σ_1= diag(0.540744, 0.664762, 0.317168, 0.304536, 0.294261, 0.419682)

Σ_2 =diag(0.008511, 0.096996, 0.006034, 0.005086, 0.015841, 0.002275)

Σ_3 =diag(0.161632, 0.000816, 0.00000049, 0.00000389, 0.006945, 0.0000027)

(2) Parameter Optimization of the Baum–Welch Algorithm

The convergence curve of the Baum–Welch algorithm is shown in Figure 3:

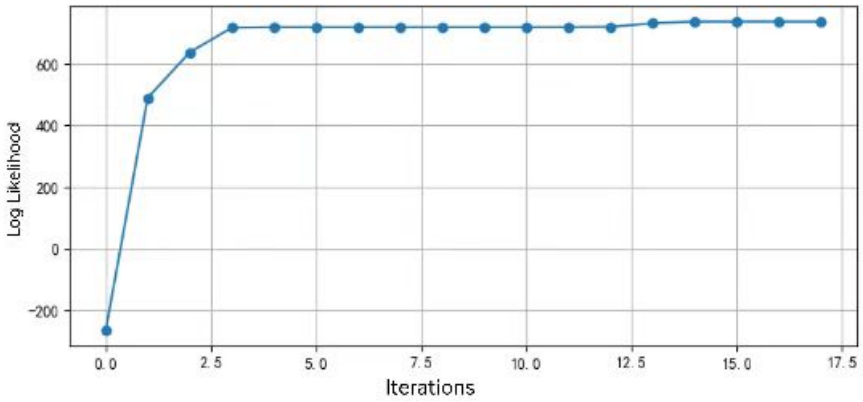


Figure 3. Convergence curve of the Baum–Welch algorithm

After the 18th iteration, the log-likelihood of the Baum–Welch algorithm stabilized at approximately 737.44, indicating that the algorithm has converged. At this point, the mean vector $\mu_i$of the Gaussian parameter emission distribution and the covariance matrix $\Sigma_i$for each state are:

$$\mu_0 = \begin{pmatrix} -0.8355 \\ -0.2982 \\ 0.8033 \\ 0.8116 \\ -0.7973 \\ 0.8009 \end{pmatrix} \mu_1 = \begin{pmatrix} 0.1382 \\ 2.4166 \\ 0.1372 \\ 0.0810 \\ -0.1936 \\ 0.0398 \end{pmatrix} \mu_2 = \begin{pmatrix} 1.6580 \\ -0.1319 \\ -1.1207 \\ -1.1188 \\ 1.1068 \\ -1.1109 \end{pmatrix} \mu_3 = \begin{pmatrix} 0.8256 \\ -0.3958 \\ -1.1912 \\ -1.1842 \\ 1.2123 \\ -1.1460 \end{pmatrix}$$

$$\sum_0 = \begin{pmatrix} 0.001455 & 0 & 0 & 0 & 0 & 0 \\ 0 & 0.367872 & 0 & 0 & 0 & 0 \\ 0 & 0 & 0.235455 & 0 & 0 & 0 \\ 0 & 0 & 0 & 0.236074 & 0 & 0 \\ 0 & 0 & 0 & 0 & 0.226267 & 0 \\ 0 & 0 & 0 & 0 & 0 & 0.271548 \end{pmatrix}$$

are denoted as:

Σ_0= diag(0.001455, 0.367872, 0.235455, 0.236074, 0.226267, 0.271548)

Σ_1 =diag(0.579433, 0.616887, 0.327270, 0.314858, 0.299020, 0.449439)

Σ_2 =diag(0.009396, 0.097786, 0.006863, 0.005917, 0.016642, 0.003105)

Σ_3 =diag(0.161850, 0.001294, 0.000477, 0.000481, 0.007429, 0.000479).

4.3. Analysis of Results

For the four stages of the sintering process (preheating, combustion, sintering, and cooling), a 4×4 confusion matrix was constructed, where the rows represent the true classes and the columns represent the predicted classes. Each element Cij in the matrix indicates the number of samples with true class i that were predicted as class j.

$$C_{ij} = \begin{pmatrix} 49 & 0 & 0 & 0 \\ 2 & 5 & 0 & 0 \\ 0 & 0 & 14 & 0 \\ 0 & 0 & 1 & 18 \end{pmatrix}$$

The confusion matrix shows that the model correctly identified all 49 preheating states. Of the 7 combustion states, 5 were correctly identified, while 2 were misclassified as preheating states. All 14 cooling states were correctly identified, and of the 19 cooling states, 18 were correctly identified, with the remaining 1 misclassified as a combustion

state, as shown in Table 1.

Table 1. Classification Performance of the Model

State	Precision	Recall	F1-score	Support
Preheating	0.9608	1.0000	0.9800	49
Combustion	1.0000	0.7143	0.8333	7
Cooling	0.9333	1.0000	0.9655	14
Sintering	1.0000	0.9474	0.9730	19

The classification performance of the model is shown in Table 1, where precision measures the proportion of samples predicted to belong to a certain class that actually belong to that class, recall measures the proportion of samples that actually belong to a certain class that are correctly identified, and the harmonic mean of the two is the F1 score (F1-score). Support indicates the actual number of samples in the test set for each class.

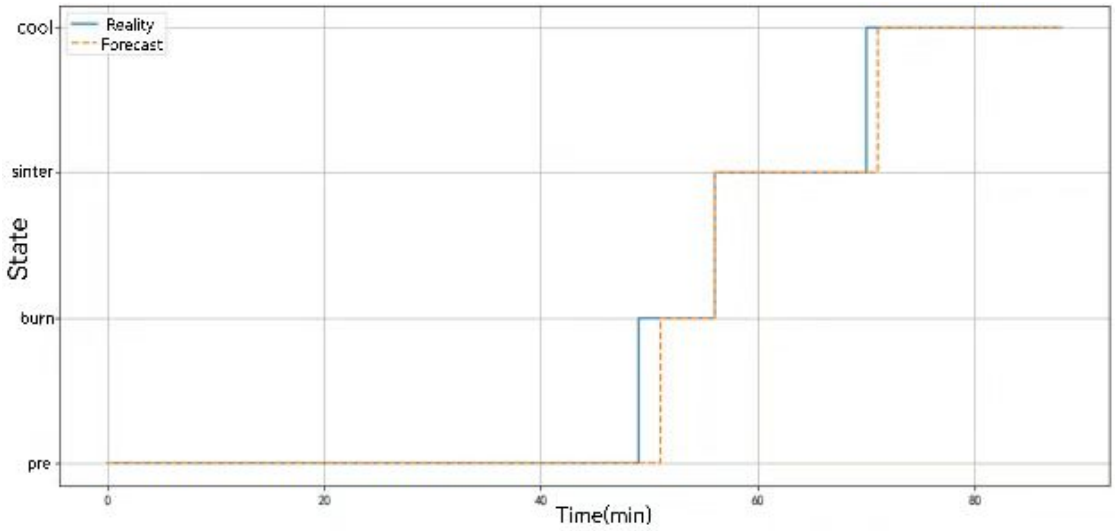


Figure 4. Comparison of Actual and Predicted States

The results indicate that the model demonstrates exceptional ability to distinguish between the three stages of "preheating," "sintering," and "cooling," with both precision and recall approaching 100% and F1 scores exceeding 0.98; the overall classification accuracy reached 96.63%. Overall, the model performs excellently and can provide reliable support for the real-time identification of each stage of the sintering process and the determination of the cooling timing. Using data from minutes 10 to 14 as observation data, the prediction results are shown in Figure 4. The model predicted that the cooling state would begin 57 minutes later, differing from the actual situation by only 1 minute; the overall accuracy of the state prediction model reached 91.55%.

5. Conclusion

Based on an analysis of the temperature and concentration characteristics of flue gas emissions during the four stages of the sintering process—preheating, combustion, sintering, and cooling—this study proposes a numerical model for characterizing the sintering state based on a Gaussian HMM model, taking into account the emission characteristics of each flue gas component. The model employs a combination of the forward-backward algorithm and the Baum-Welch algorithm to optimize the parameters of the Gaussian emission distribution, and utilizes the Viterbi decoding strategy to dynamically track the transition paths of the sintering thermal state. The computational results indicate that the model's accurate calculation of the sintering thermal state provides reliable support for the precise identification of the thermal state during the sintering process.

6. Project Support

Undergraduate Innovation and Entrepreneurship Training Program (X2024117).

References

[1] Fernández-González D, Ruiz-Bustinza I, Mochón J, et al. Iron ore sintering: Process[J]. Mineral Processing and Extractive Metallurgy Review, 2017, 38(4): 215-227.

[2] Zhao Jiapei. Numerical Simulation and Experimental Validation of the Iron Ore Sintering Process [D]. Zhejiang University, 2012.

[3] Long Hongming, Fan Xiaohui, Mao Xiaoming, et al. Study on the Thermal State of the Sintering Process Based on Side Plate Temperature Measurement [J]. Iron and Steel, 2009, 44(07): 15-19.

[4] Jing Kai, Wang Xuming, Li Yang, Wang Hongwen. Sintering End-Point Prediction Based on ANFIS [J]. Sintering and Pelletizing, 2011, 36(05): 8-11.

[5] Wang Hongwen, He Longxiang. Research on the Application of Wavelet Analysis Time Series Algorithms in Sintering End-Point Prediction [J]. Computer Measurement and Control, 2013, 21(01): 27-29+38.

[6] Ding Yuan, Wang Bin, Yan Jinchong, Pan Bi. Prediction of Sintering End Point Based on a Two-Dimensional Interval Autoregressive Model [J]. Sintering and Pelletizing, 2017, 42(03): 1-6.

[7] Wang Fubin, Liu Hefei, He Jianghong, Wu Chen. Analysis of Sintering Operating Parameters and Construction of a Sintering Behavior Model [J]. Sintering and Pelletizing, 2020, 45(06): 29-34+68.

[8] YANG C, YANG C J, ZHANG X M, et al. Multi-source information fusion for autoformer soft sensor modeling of FeO content in iron ore sintering process [J]. IEEE Transactions on Industrial Informatics, 2023, 19 (12): 11584–11595.

[9] Fan Xiaohui, Huang Xiaoxian, Chen Xuling, et al. Research Progress on Intelligent Control of the Sintering Process [J]. Sintering and Pelletizing, 2023, 48(06): 1-9+21.

[10] Yang Jing, Huang Zaijing, Mo Zhaoyu, et al. Application of an Intelligent Sintering Condition Recognition and Online Quality Prediction System [J]. Shanxi Metallurgy, 2024, 47(07): 191–194.

[11] Song Qifeng, Fang Yong. Parameter Estimation of Non-stationary Sources Based on Hidden Markov Models [J]. Computer Applications and Software, 2013, 30(09): 67-70.

[12] Varadharajan A A, Vaddi R S, Ramasubramanian G K. Improved Diverse Gaussian HMM and SVM ML Technique for Sensor Fault Detection and Classification in Air Quality Monitoring Systems [J]. Ingénierie des Systèmes d'Information, 2023, 28(1): DOI:10.18280/ISI.280111.

[13] Chen Junxia, Liu Ziyu. A Study on the Isolated Word Algorithm Based on the Baum-Welch Algorithm HMM Model [J]. Journal of Hebei University of Science and Technology, 2015, 36(01): 52-57.

[14] Song Yanhong, Wang Zhicheng. The Viterbi Algorithm for Partially Observable Hidden Markov Models [J]. Acta Mathematica Sinica (Chinese Edition), 2024, 67(03): 500-510.